Numerical Heat Transfer, Part B, 51: 351–374, 2007

ISSN: 1040-7790 print/1521-0626 online
DOI: 10.1080/10407790601144730

ON A MUSHY CELL TRACKING METHOD FOR SIMULATING GALLIUM MELTING

Yih-Jena Jan
National Kao-Hsiung Marine University, Taiwan, Republic of China

Tony Wen-Hann Sheu
Department of Engineering Science and Ocean Engineering, National Taiwan University, Taiwan, Republic of China

Zhen-Yu Hsu and Fang-Pang Lin
Department of Mechanical Engineering, National Chiao Tung University, Taiwan, Republic of China

Gallium melting in a rectangular cavity heated from the side wall has been extensively studied. Since the previously simulated results were not consistent and the myth of a grid-converged solution remained, we reexamine this problem using the thermally driven mushy cell tracking method to clarify whether the solution is physically correct. In the study, the computational domain is separated into solid-phase and liquid-phase regions, with the mushy cell placed in between. The governing equations for the thermofluid transport are expressed in terms of the primitive variables and are discretized in the stationary unstructured grid using the finite-volume formulation. The mushy cell tracking equation is derived under the mass and energy balance laws to capture the mushy cell front. With the variables located in the cell centers, the distinguishing characteristic of the present tracking algorithm lies in the specification of constant melting or freezing temperature at the center of the mushy cells without consideration of the curvature and normal velocity effects in the dendritic solidification. Thanks to this feature, a straightforward and accurate evaluation of the boundary conditions at the interface of the mushy, solid, and liquid cells becomes feasible. The predicted moving interface and thermofluid field of gallium melting are shown to agree well with the results from other numerical solutions.

1. INTRODUCTION

In the past two decades, numerous studies of phase-change problems encountered in natural environments and processing industries have been made by computational fluid dynamics scientists [7, 9, 14]. This class of problems is characterized by some internal boundaries or interfaces, across which the physicchemical properties can change sharply. Nonlinear physical complexities emerge from a wide range of

Received 2 October 2006; accepted 11 November 2006.
The authors would like to thank the National Science Council of Taiwan for funding this research (Project NSC 95-221-E-022-016).
Address correspondence to Yih-Jena Jan, National Kaohsiung Marine University, No. 482, Jhong Jhou 3rd, Cijin District, Kaohsiung, Taiwan, 805. E-mail: yjjan@mail.nkmu.edu.tw

NOMENCLATURE

A_f	outward area vector for the $face_f$	δt	time step
P	pressure	ν	kinetic viscosity
St	Stefan number, $C_s \Delta T / \Delta H$	ρ	density
t	time	$\underline{\nabla}$	gradient operator
u_i	velocity component along the i-direction	Ω_0	domain of $cell_0$
$\underline{U}$	velocity vector	$\|\Omega_0\|$	volume of Ω_0
$\underline{U}_f$	face velocity vector		

time and space scales. In addition, geometric complexities, such as multibody configurations and bodies with complex shapes, can further complicate the analysis. The moving interface itself is considered as a part of the solution process for solving the system of equations governing the behavior of the thermofluid flow field. Free-and moving-boundary problems are normally difficult to analyze because of their geometric and physical complexities, among other factors. Analytic solutions for this class of problems are only available for very few cases with simple geometry [9, 14]. With the advent of high-speed computers, numerical capturing of the time-varying interfaces has gradually become feasible. In the literature, the methods employed for solving free/moving-boundary problems can be classified into the enthalpy-based [10, 11] and moving = particle [12] methods. Shyy [7] has given a detailed review of these methods.

When a numerical method is applied to solve problems involving solidification of liquid and melting of solid, the working equations for describing the conservations of mass, momentum, and energy along with the tracking of the moving interface are required. In this study, the cell-by-cell thermally driven mushy cell tracking algorithm [5, 6] is applied to simulate 1 D solidification and 2 D tin melting. After investigating these two benchmark tests, the gallium melting problem is investigated. The computational domain is separated into solid-phase and liquid-phase regions, with the mushy cell placed in between. The transport phenomenon in the solid-phase region is governed by the stable diffusion process, while the transport phenomenon of the liquid-phase region is governed by the conditionally stable convection-diffusion process. The movement of the interface, which is referred to as the computational mushy cell, for the current two-phase problem is governed by the mass and energy balance principles. A detailed description of the method and its application to various fields can be found in [5, 6]. The distinguished characteristic of the present algorithm is the specification of constant melting or freezing temperature without considering curvature and normal velocity effects in the dendritic solidification [22]. Thanks to this embedded feature, one can easily and accurately evaluate the boundary conditions at the interface between the mushy, solid, and liquid cells. In comparison with other methods, the mushy cell tracking algorithm has the following distinguishing features [5].

1. The volume-averaged property $\langle F \rangle_m$ is introduced.
2. Solidification or melting time is defined as a function of $\langle F \rangle_m$.
3. Evaluation of $\partial T / \partial t$ in the mushy cells is circumvented.

4. The field variables for both liquid and solid phases are solved without introducing any source term involving the volume-averaged $\langle F \rangle_m$ explicitly.
5. The size of the region of $\langle F \rangle_m$ is controlled by the mushy cell, and can be reduced to a local point of the moving front.
6. The algorithm is mainly controlled by a conduction-type equation, and there is no need to solve for the temperature in the mushy cells since a constant melting temperature condition is specified at the interfaces between the mushy and either solid or liquid cells.
7. The mushy cells separate the domain into liquid and solid zones. Consequently, the field variables are solved in a phase-by-phase and cell-by-cell manner.

To validate the present algorithm, both the 1-D solidification without consideration of convection [14] and the melting of tin in a rectangular cavity with consideration of convection effect [1–4, 11, 13, 15, 16] will be investigated. The first problem is the so-called Stefan problem. The predicted interface location, which has been known to be amenable to analytical solution, will be used to access the proposed numerical model. The gallium melting problem has been studied experimentally [1] and numerically [2–4]. Hannoun et al. [4] gave an excellent review of the gallium melting problem and tried to resolve some previously known controversies. This problem will be reexamined in this study using the mushy cell tracking algorithm with an aim of clarifying the afore-mentioned controversial problem.

2. WORKING EQUATIONS

The solidification problem is sometimes referred to as the Stefan problem, since this problem was first published by Stefan [14] to study the thickness of the polar ice cap. This classical problem considers the energy conservation in the domain Ω by dividing it into three distinct domains, Ω_s (solid zone), Ω_m (mushy zone), and Ω_L (liquid zone), where $\Omega_s \cup \Omega_m \cup \Omega_L = \Omega$. The flow and energy conservation equations are expressed as

$$\underline{\nabla} \bullet \underline{U} = 0 \qquad \text{in } \Omega_L \tag{1a}$$

$$\rho_L \left[\frac{\partial \underline{U}}{\partial t} + \underline{\nabla} \bullet (\underline{U}\underline{U}) \right] = -\underline{\nabla} P + \underline{\nabla} \bullet \underline{\underline{\tau}} - \rho_L \underline{g} \beta_T (T - T_{\text{ref}}) \qquad \text{in } \Omega_L \tag{1b}$$

$$\rho_L C_P \left[\frac{\partial T}{\partial t} + \underline{\nabla} \bullet (\underline{U} T) \right] = \underline{\nabla} \bullet k_L \underline{\nabla} T \qquad \text{in } \Omega_L \tag{1c}$$

$$\rho_S C_P \frac{\partial T}{\partial t} = \underline{\nabla} \bullet k_S \underline{\nabla} T \qquad \text{in } \Omega_S \tag{1d}$$

where

$$\underline{\underline{\tau}} \equiv \mu \left[(\underline{\nabla} \underline{U}) + (\underline{\nabla} \underline{U})' \right] - \frac{2\mu}{3} \underline{\nabla} \bullet \underline{U} \qquad \text{in } \Omega_L \tag{2}$$

It should be noted that the current study is investigated under the isothermal moving-interface restriction. The internal boundary condition is specified as

$$T = T_m \qquad \text{in } \Omega_m(t) \cup \partial\Omega_m(t) \tag{3}$$

The subscripts s, L, and m denote the solid, liquid, and mushy states, respectively. Other physical properties involved are the density ρ, specific heat C_P, gravity acceleration $\underline{g}$, temperature T, dynamic viscosity μ, thermal conductivity k, and the thermal expansion coefficient β_T. In Eq. (1), $\underline{U}$ is the fluid velocity and P is the pressure.

When considering phase-change problems without taking into account convection, the equation for the thermal energy can be reduced to one similar to that for solid heat conduction. To describe the movement of the mushy cell, one additional equation is needed in order to account for the energy balance at the interface of the mushy cell. When the moving-particle method is used to trace the front propagation, the Stefan condition [14] should be valid at the solid/liquid interface for truly representing the solidification process,

$$\rho_s(\Delta H)\underline{W} \bullet \underline{n} = k_s \underline{\nabla} T_s \bullet \underline{n} - k_L \underline{\nabla} T_L \bullet \underline{n} \tag{4}$$

In the above equation, ΔH denotes the latent heat of solidification. The vector $\underline{n}$ is the outward normal vector of the moving front, and $\underline{\nabla} T_L \bullet \underline{n}$ and $\underline{\nabla} T_s \bullet \underline{n}$ denote the normal derivatives of T in the liquid and solid regions, respectively. $\underline{W}$ is the velocity of the moving front. It should be noted that Eq. (4) corresponds to the constant melting or frozen temperature criterion. When using this front-capturing method, the computational time and memory requirements can be excessive. However, both the computational time and memory can be significantly reduced in the mushy cell tracking approach presented later on.

During solidification, the mushy cell tracking equation will be derived within the nonmoving framework using the control-volume method. The equations for the conservation of mass and energy can be written in integral forms as follows:

$$\frac{\partial}{\partial t}\int_{\Omega_m} \rho \, d\Lambda + \oint_{\partial\Omega_m} \rho(\underline{U} - \underline{W}_m) \bullet d\underline{A} = 0 \tag{5}$$

$$\frac{\partial}{\partial t}\int_{\Omega_m} \rho H \, d\Lambda + \oint_{\partial\Omega_m} \rho H(U - \underline{W}_m) \bullet d\underline{A} = \oint_{\partial\Omega_m} \underline{q} \bullet d\underline{A} \tag{6}$$

In the above equations, $\underline{W}_m$ is the control-surface velocity, which is zero for a fixed control volume, Ω_m is the fixed control volume, and $\underline{q}$ is the conduction heat flux. Here, the following two important assumptions will be made:

1. No flow is allowed to proceed between the mushy cells. Actually, the mushy cell is treated as a porous medium with a fairly high resistance to the flow.
2. Across the interface, no temperature gradient is allowed to take place because the temperature of each mushy cell is specified as T_m. Taking the mushy cell shown in

Figure 1 as an example, the mass and energy equations can be expressed as

$$\|\Omega_m\| \frac{\partial}{\partial t} \langle \rho \rangle_{\Omega_m} + \sum (\rho_L (\underline{U}_{mL} - \underline{0}) \bullet \underline{A}_{mL}) = 0 \tag{7}$$

$$\begin{aligned} \|\Omega_m\| \frac{\partial}{\partial t} \langle \rho H \rangle_{\Omega_m} + \sum (\rho_L H_{mL} (\underline{U}_{mL} - \underline{0}) \bullet \underline{A}_{mL}) \\ = \sum (k_s \underline{\nabla} T_s \bullet \underline{A}_{ms}) + \sum (k_L \underline{\nabla} T_L \bullet \underline{A}_{mL}) \end{aligned} \tag{8}$$

In the above equations, $\underline{A}_{mL}$ is the outward normal vector from the cell Ω_m and is directed toward the neighboring liquid cell. The associated enthalpy H_{mL} is evaluated at the face center shown in Figure 1. $\underline{U}_{mL}$ is the convective velocity at the face between the mushy and liquid cells. The volume-averaged solid fraction $\langle F \rangle_m$ is defined to be the volumetric integration of the local solid fraction F and is given as

$$\langle F \rangle_m \equiv \frac{1}{\|\Omega_m\|} \int_{\Omega_m} F \, d\Lambda \tag{9}$$

It is noted that $\langle \rho \rangle_{\Omega_m}$ is a time-dependent property, since $\langle F \rangle_m$ varies with the time. Thus, Eq. (7) can be written as

$$\sum \rho_L \underline{U}_{mL} \bullet \underline{A}_{mL} = -\|\Omega_m\| \frac{\partial}{\partial t} \langle \rho \rangle_{\Omega_m} \tag{10}$$

It is worth noting that Eq. (10) is the constraint prescribed at the interface of the mushy and liquid cells. The velocity at this interface is initially estimated to be the averaged velocity magnitudes for the two adjacent cells. Each estimated velocity is then corrected by using a scaling factor such that the net mass flow rate due to the corrected velocities becomes exactly equal to the right-hand side of Eq. (10).

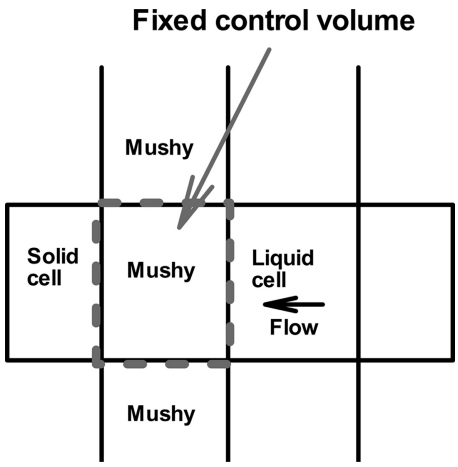

Figure 1. Mushy cell viewed as a fixed control volume.

The interface velocity thus obtained serves as the boundary condition for the flow simulation in the liquid region.

To complete the derivation of mushy cell tracking equation, one additional condition relating to the enthalpy of solid or liquid is commonly required,

$$\begin{cases} H_L \equiv C_s T_m + \underbrace{\Delta H}_{\text{Latent heat}} + C_L(T_L - T_m) & \Omega_L \cup \partial\Omega_{mL} \\ H_s \equiv C_s T_s & \Omega_s \cup \partial\Omega_{ms} \end{cases} \tag{11}$$

It should be noted that the interface temperature T_{mL} is set as T_m in Eq. (11), which leads to $H_{mL} = C_s T_m + \Delta H$. For convenience, it can be assumed that $T_{ms} = T_m$. These specifications will provide the essential boundary condition at the interface of the mushy and liquid (or solid) cells. In other words, once the mushy cell is formed, its temperature becomes the same as T_m. Combining Eqs. (8), (10), and (11), we have

$$\begin{aligned} &\|\Omega_m\| \left(\frac{\partial}{\partial t} \langle \rho H \rangle_{\Omega_m} - H_{mL} \frac{\partial}{\partial t} \langle \rho \rangle_{\Omega_m} \right) \\ &\quad = \sum (k_s \langle \underline{\nabla} T_s \rangle \bullet \underline{A}_{ms}) + \sum (k_L \langle \underline{\nabla} T_L \rangle \bullet \underline{A}_{mL}) \end{aligned} \tag{12}$$

The volume-averaged properties $\langle \rho H \rangle_{\Omega_m}$ and $\langle \rho \rangle_{\Omega_m}$ seen above are given as follows:

$$\begin{cases} \langle \rho H \rangle_{\Omega_m} = \underbrace{\langle F \rangle_m (\rho_s C_s T_m)}_{\text{Enthalpy of solid part}} + \underbrace{(1 - \langle F \rangle_m) \rho_L (C_s T_m + \Delta H)}_{\text{Enthalpy of liquid part}} \\ \langle \rho \rangle_{\Omega_m} = \langle F \rangle_m \rho_s + (1 - \langle F \rangle_m) \rho_L \end{cases} \tag{13}$$

Under these conditions, Eq. (12) can be simplified as

$$\begin{aligned} &\|\Omega_m\| \left\{ \begin{array}{c} \left[\rho_s C_s T_m \frac{\partial \langle F \rangle_m}{\partial t} - \rho_L (C_s T_m + \Delta H) \frac{\partial \langle F \rangle_m}{\partial t} \right] \\ -(C_s T_m + \Delta H) \left(\rho_s \frac{\partial \langle F \rangle_m}{\partial t} - \rho_L \frac{\partial \langle F \rangle_m}{\partial t} \right) \end{array} \right\} \\ &\quad = \sum (K_s \langle \underline{\nabla} T_s \rangle \bullet \underline{A}_{ms}) + \sum (K_L \langle \underline{\nabla} T_L \rangle \bullet \underline{A}_{mL}) \end{aligned}$$

or

$$-\|\Omega_m\| (\rho_s \Delta H) \frac{\partial \langle F \rangle_m}{\partial t} = \sum (K_s \langle \underline{\nabla} T_s \rangle \bullet \underline{A}_{ms}) + \sum (K_L \langle \underline{\nabla} T_L \rangle \bullet \underline{A}_{mL}) \tag{14}$$

Further manipulation of Eq. (14) results in

$$\|\Omega_m\| \frac{\partial \langle F \rangle_m}{\partial t} = \sum \left(\frac{-K_s \langle \underline{\nabla} T_s \rangle \bullet \underline{A}_{ms}}{\rho_s \Delta H} \right) + \sum \left(\frac{-K_L \langle \underline{\nabla} T_L \rangle \bullet \underline{A}_{mL}}{\rho_s \Delta H} \right)$$

or

$$\|\Omega_m\| \frac{\partial \langle F \rangle_m}{\partial t} = \sum_{f_{i=L,s}} \left(\frac{-K_i}{\rho_s \Delta H} \langle \underline{\nabla} T_i \rangle \bullet \underline{A}_f \right) \tag{15}$$

where $\underline{A}_f$ is the outward normal vector of face$_f$ from the mushy cell Ω_m and is directed toward the neighboring cell of i (solid or liquid phase). Only the thermal diffusion fluxes from the liquid and solid phases will be included, due to the above two main mentioned assumptions.

As stated in Part I of [5, 6], the main reason for choosing the mushy cell tracking equation is the minimum time step which is applicable to update $\langle F \rangle_m$ for every mushy cell. This minimum time step is determined by scrutinizing every mushy cell so that it can be used to define the new front location at the updated time level. In addition, the associated essential boundary conditions are as follows:

$$\begin{cases} T_{mL} = T_{ms} = T_m \\ \sum \rho_L \underline{V}_{mL} \bullet \underline{A}_{mL} = -\|\Omega_m\| \dfrac{\partial}{\partial t} \langle \rho \rangle_{\Omega_m} \end{cases} \tag{16}$$

where T_{mL} is the temperature between the mushy and liquid cells. It is worth noting that the advancing length of the moving front is limited by the length of a cell in a cell-by-cell manner to update $\langle F \rangle_m$ for every mushy cell. The candidates for the mushy cells can be easily identified by examining the neighbors (in liquid state) of the newly solidified mushy cells. Thus, the mushy cells can be advanced in a cell-sby-cell manner as illustrated in Figure 2. In a similar manner, one can derive the well-known Stefan condition shown in Eq. (4) by the moving-control-volume method to get the essential temperature boundary conditions at the interface between mushy and liquid or solid phases [6].

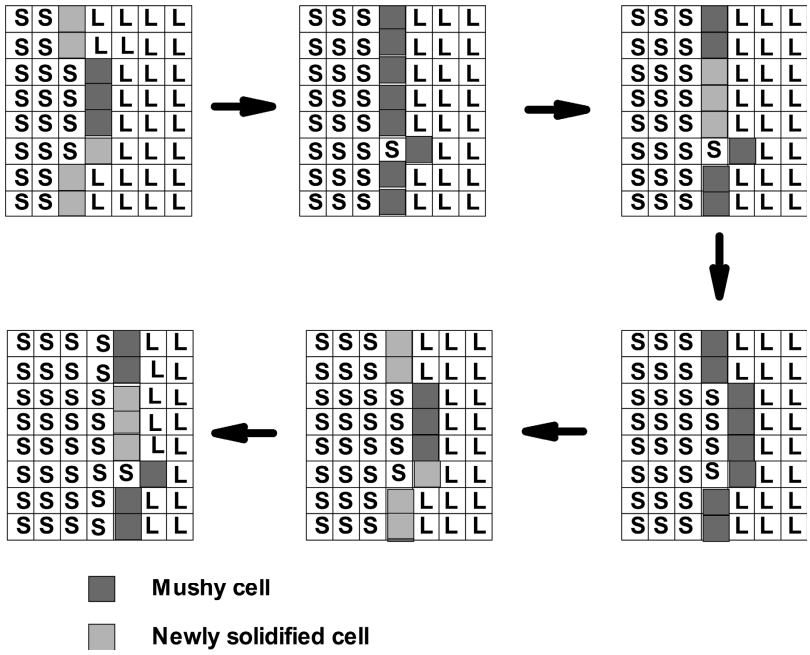

Figure 2. Illustration of the mushy cell advancing.

3. NUMERICAL METHOD

The domain to be investigated is initially subdivided into several convex polyhedrons or cells. The boundaries and vertices of the cells are referred to as the faces and nodes, respectively. Neighboring cells are defined as those sharing a common face. All transport variables are stored at the cell centers. The resulting cells are known as the nonstaggered cell-centered control volumes, as illustrated in Figure 3. The thermally driven mushy cell movement is described in Figure 2 for the sake of illustration. When applying the cell-by-cell thermally driven mushy cell tracking algorithm, it is worth noting that the convection terms near the walls are still retained because all variables are evaluated at the cell center rather than on a cell boundary. It is also worthwhile to note the following advantages of storing field variables at the cell center:

1. The mushy cell can be easily identified without interpolating or extrapolating the moving front. Therefore, the computational time can be considerably reduced.
2. Heat flux into the mushy cell can be easily calculated.
3. The number of faces of one particular cell is fixed so that the matrix solver can be easily dealt with.
4. The boundary temperature along the moving front could be easily set as the mushy temperature at the cell center instead of the melting or frozen temperature at the front. The interpolated or extrapolated procedures can therefore be omitted.

The transport equation for a scalar quantity Φ can be cast into the following form by choosing the appropriate Γ and S_Φ:

$$\frac{\partial(\rho\Phi)}{\partial t} + \frac{\partial}{\partial x_i}(\rho u_i \Phi) = \frac{\partial}{\partial x_i}\left(\Gamma \frac{\partial \Phi}{\partial x_i}\right) + S_\Phi \tag{17}$$

where Γ is the transport coefficient such as the viscosity μ and the ratio $\alpha_L = k_L/C_L$.

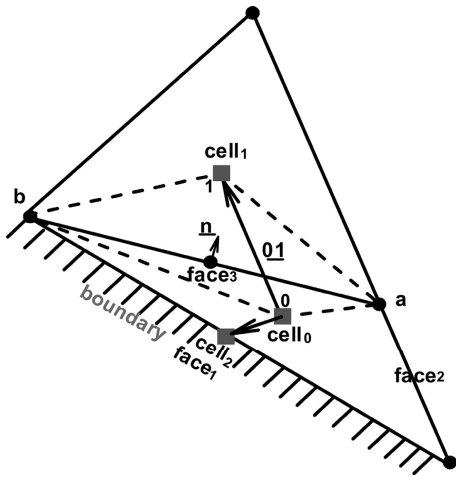

Figure 3. Diagram of the unstructured finite-volume and the notations used.

Integration of Eq. (17) over the control volume Ω_0, schematic in Figure 3, can result in the following equation:

$$\frac{\|\Omega_0\|\rho\Phi_0^{n+1}}{\delta t} + \sum_f J_f\Phi_f = \sum_f D_f + S_\Phi\|\Omega_0\| + \frac{\|\Omega_0\|\rho\Phi_0^n}{\delta t} \tag{18}$$

The mass flow rate J_f is defined to be larger than zero for the fluid leaving Ω_0. D_f represents the diffusion transport through the face "face$_f$". $\|\Omega_0\|$ is the volume of the domain Ω_0. In Eq. (18), the Euler time-stepping method is used to render first-order temporal accuracy.

In the absence of a line structure, the field variable and its derivatives cannot be obtained directly from the Taylor series expansion. To overcome this difficulty, several gradient reconstruction strategies have been proposed [24–26]. Among them, the CVFEM method [18] employed the shape function, and another approach used the least-squares technique [24]. These techniques are, however, quite expensive and are dependent on the cell shape. If a shape-independent formulation [23] for the cell gradients can be devised by virtue of the divergence theorem, a hyper-order-accurate value of Φ_f at the cell face could be calculated from the following formula:

$$\Phi_f = \underbrace{\Phi^{n+1}_{\text{upwind}}}_{\text{1st term}} + \underbrace{\underline{\nabla}\Phi^n_{\text{upwind, r}} \bullet d\underline{r}}_{\text{2nd term}} \tag{19}$$

In the above equation, $d\underline{r}$ denotes the vector with direction from the centroid of an upwind cell to the center of the face. The value of $\Phi^{n+1}_{\text{upwind}}$ is obtained from an upwind cell, and the reconstructed gradient $\underline{\nabla}\Phi^n_{\text{upwind, r}}$ is evaluated from the upwind cell at the time instant t_n. Note that all field variables are treated implicitly, while their gradients are evaluated explicitly.

The transport flux D_f due to heat conduction through face$_f$ is derived below based on the Gauss divergence theorem:

$$D_f \equiv \alpha_i\langle\underline{\nabla}T\rangle_f \bullet \underline{A}_f \tag{20}$$

where the thermal diffusivity α_i is defined as $\alpha_i = k_i/C_i$. In Eq. (20), the temperature flux across a face can be generally expressed as [23]

$$\langle\underline{\nabla}T\rangle_f \bullet \underline{A}_f = \underbrace{(T_1 - T_0)\frac{\underline{A}_f \bullet \underline{A}_f}{\underline{A}_f \bullet \underline{01}}}_{\text{first term}} + \underbrace{\langle\overline{\underline{\nabla}}T\rangle_f \bullet \left(\underline{A}_f - \underline{01}\frac{\underline{A}_f \bullet \underline{A}_f}{\underline{A}_f \bullet \underline{01}}\right)}_{\text{Second term}} \tag{21}$$

where

$$\langle\overline{\underline{\nabla}}T\rangle_f = \frac{1}{2}(\langle\underline{\nabla}T\rangle_0 + \langle\underline{\nabla}T\rangle_1) \qquad \text{and} \qquad \langle\underline{\nabla}T\rangle_0 = \frac{1}{\|\Omega_0\|}\sum_f T_f\underline{A}_f$$

At a face$_f$, $\langle\overline{\underline{\nabla}}T\rangle_f$ and T_f are taken to be the averaged quantities of the two adjacent cells. The face vector $\underline{A}_f$ is directed outward and is normal to face$_f$ for Ω_0, and $\underline{01}$ is

the distance vector measured from the center of Ω_0 to the center of Ω_1, which is the neighboring cell of Ω_0 shown in Figure 3. The first term in Eq. (21) is of the first-order-accurate type, and the second term is known as its hyper-order (super-linear) correction. It will be addressed that second-order accuracy could be achieved in an orthogonal and quadrilateral cell later on.

Based on Eq. (21), the following linear system of equations for the field variable T at the cell centers can be derived in the solid phase or liquid phase under the motion-free condition:

$$\left(\frac{\rho\|\Omega_0\|}{\delta t}+B_0\right)T_0^{n+1}-\sum_{\mathrm{nb}}B_{\mathrm{nb}}T_{\mathrm{nb}}^{n+1}=S_0+\frac{\rho\|\Omega_0\|}{\delta t}T_0^n$$
$$B_{\mathrm{nb}}=\alpha_i\frac{\underline{A}_f\bullet\underline{A}_f}{\underline{01}\bullet\underline{A}_f}\qquad B_0=\sum_{\mathrm{nb}}B_{\mathrm{nb}} \tag{22}$$

Here, the summation is made over all the neighbors "nb" of Ω_0. The source term S_0 contains the super-linear term, such as the secondary diffusion flux terms in Eq. (21). The diffusion fluxes at the boundaries are also included in S_0, and T is applied at the center of the boundary. When solving Eq. (22), the interface temperature between the mushy and liquid and solid cells is specified by the constant melting or freezing temperature, respectively. The boundary diffusion flux can then be treated similarly to that at an interior face using Eq. (21). The flux D_2 on a boundary schematic in Figure 2 can be written as

$$D_2=\underbrace{\alpha_i(T_2-T_0)\frac{\underline{A}_f\bullet\underline{A}_f}{\underline{A}_f\bullet\underline{02}}}_{\text{first term}}+\underbrace{\alpha_i\langle\overline{\underline{\nabla}}T\rangle_f\bullet\left(\underline{A}_f-\underline{02}\frac{\underline{A}_f\bullet\underline{A}_f}{\underline{A}_f\bullet\underline{02}}\right)}_{\text{Second term}} \tag{23}$$

where T_2 is evaluated at the center of the boundary face and vector $\underline{02}$ is measured from the center of the cell Ω_0 to the centroid of the boundary face. For the case with Dirichlet-type boundary condition, the first term in Eq. (23) is treated implicitly and will be included in the left-hand side of Eq. (22). As for the second term in Eq. (23), it is included in the right-hand side of Eq. (22). For the case with Neumann boundary condition, the specified flux can be implemented directly in the control-volume integration.

After assembling all the discretized terms, including the convection, diffusion, and source terms, the following linear system of equations for Φ can be derived at each cell center in the liquid phase containing the convection effect:

$$\frac{\|\Omega_0\|\rho\Phi_0^{k+1}}{\delta t}+B_0\Phi_0^{k+1}-\sum_{\mathrm{nb}}B_{\mathrm{nb}}\Phi_{\mathrm{nb}}^{k+1}=S_0+\frac{\|\Omega_0\|\rho\Phi_0^k}{\delta t} \tag{24}$$

Here, $\|\Omega_0\|$ is the volume of Ω_0. The notation nb denotes the number of neighboring cells of Ω_0. The source term S_0 contains the volumetric source of Φ and the deferred correction of Φ_f, as shown in Eq. (19). The flux contributions at boundaries are included in S_0, and B_0 is the coefficient containing the contributions from the

convection and diffusion fluxes in the liquid phase considering the convection effect. The superscript k denotes the k_t^{th} sub-time step in the n time step.

Since the pressure and the velocity components are stored at the cell centers, the mass flow rate J_f, which is obtained by averaging the cell center velocities, is prone to oscillatory modes and checkerboard pressure patterns. To overcome these drawbacks, a scheme [17, 23, 27] similar to that of Rhie and Chow [28] will be used. At the face "face$_f$" schematic in Figure 1, the mass flow rate is determined by

$$J_f = \rho_f \underline{A}_f \bullet \left(\frac{\underline{U}_0^* + \underline{U}_1^*}{2}\right) - \underbrace{\frac{\rho_f(\|\Omega_0\| + \|\Omega_1\|)}{\left(\rho\|\Omega_0\|/\delta t + B_0\right) + \left(\rho\|\Omega_1\|/\delta t + B_1\right)}\left[\left((P_1 - P_0) - \langle\underline{\nabla}P\rangle_f \bullet \underline{01}\right)\frac{\underline{A}_f \bullet \underline{A}_f}{\underline{A}_f \bullet \underline{01}}\right]}_{\text{correction term from momentum}} \tag{25}$$

where $\underline{U}^*$ is the velocity field that satisfies the momentum conservation law. B_0 is the coefficient in the discrete momentum equation for the cell Ω_0 shown in Eq. (25), $\langle\underline{\nabla}P\rangle_f$ is the averaged pressure gradient evaluated at the cell face "face$_f$," and $\underline{01}$ is the vector measured from the center of Ω_0 to the center of Ω_1.

In each momentum equation, the source term contains the pressure gradient, the thermal buoyancy force, and the stress tensor components are not included in the standard diffusion term:

$$\frac{\partial}{\partial x_j}\left(\mu\frac{\partial u_j}{\partial x_i} - \frac{2}{3}\delta_{ij}\mu\frac{\partial u_l}{\partial x_l} - \delta_{ij}P\right) - \rho g_i \beta_T (T - T_m) \tag{26}$$

Integration of Eq. (26) over the control volume Ω_0 results in the following equation:

$$\sum_f \left(\mu_f\frac{\partial u_j}{\partial x_i} - \frac{2}{3}\delta_{ij}\mu_f\frac{\partial u_l}{\partial x_l} - \delta_{ij}P_f\right)A_j + [-\rho g_i \beta_T (T - T_m)]\|\Omega_0\| \tag{27}$$

where the viscosity μ_f, the extra shear, and the pressure forces at the cell face are evaluated by averaging the cell derivatives and cell values, respectively. The buoyancy force due to thermal expansion is also evaluated at the control-volume center.

Within the SIMPLE solution framework, the pressure-correction equation can be derived as follows, according to [27]:

$$\underline{U}' = -\frac{\delta t}{\rho}\underline{\nabla}P' \tag{28}$$

$$P^{k+1} = P^k + P' \qquad \underline{U}^{k+1} = \underline{U}^k + \underline{U}' \tag{29}$$

$$\underline{\nabla} \bullet (\rho\underline{U}') = -\underline{\nabla} \bullet \left(\rho\underline{U}^k\right) \tag{30}$$

Substituting Eq. (28) into Eq. (30), the pressure-correction equation is derived as

$$\underline{\nabla}^2 P' = \frac{1}{\delta t}\underline{\nabla} \bullet \left(\rho \underline{U}^k\right) \tag{31}$$

where the superscript k represents the predictor step or the previous corrector step. After discretization and integration of Eq. (31) over the control volume Ω_0, the following discrete equation can be obtained:

$$\begin{gathered} A_0 P'_0 + \sum_{\mathrm{nb}} A_{\mathrm{nb}} P'_{\mathrm{nb}} = -\frac{1}{\delta t}\sum \left(\rho \underline{U}^k \bullet \underline{A}\right)_f + \sum_f \left[\left\langle \underline{\nabla} P' \right\rangle_f \bullet \left(\underline{A}_f - \underline{01}\frac{\underline{A}_f \bullet \underline{A}_f}{\underline{A}_f \bullet \underline{01}}\right)\right] \\ A_{\mathrm{nb}} = -\frac{\underline{A}_f \bullet \underline{A}_f}{\underline{01} \bullet \underline{A}_f} \qquad A_0 = -\sum_{\mathrm{nb}} A_{\mathrm{nb}} \end{gathered} \tag{32}$$

The above system of equations will be solved using a preconditioned conjugate gradient method. Two algorithms of the conjugate gradient (CG) type [19] are employed in the present study. The preconditioned CG method is used to solve the pressure-correction coefficient matrix equation, since it is classified to be symmetric and positive definite. The preconditioned BiCGSTAB method is selected for solving the momentum and the discretized temperature equations with convection. Once the solution of Eq. (32) is obtained through the preconditioned CG solver, both velocity and pressure fields can be updated using Eq. (29). The entire corrector step is repeated until convergence. If the boundary pressure is not known, then the Neumann-type boundary condition [8], Eq. (28), is employed along with the known boundary velocity. The solution procedures based on the liquid phase containing the convection effect for solidification are summarized as follows.

1. Define spatially the liquid phase, the mushy zone, and the solid phase. The minimum time step δt is then determined from the mushy cell tracking equation. The value of $\langle F \rangle_m$ can be then updated for each mushy cell.
2. Solve for the heat conduction equation in the solid phase with the time step δt and the governing equations in the liquid phase using the SIMPLE algorithm to determine the velocity, pressure, and temperature. To stabilize the calculation, δt is decomposed into several sub-time steps, i.e., $\delta t = \sum_s (\delta t)_s$. In the mushy cell tracking equation, the velocity is controlled by the diffusion contribution. Since a cell-by-cell approach is used to move the front by virtue of the characteristic cell length h, $(\delta t)_{\mathrm{ref}} = 0.3\left(h^2 \rho_L C_L / k_L\right)$ is currently selected as a constraint on $(\delta t)_s$, which is the sub-time step of the minimum time step δt. It is noted that $h^2 \rho_L C_L / k_L$ has the unit of time and is therefore considered as the local cell's time scale. Thus, the sub-time step $(\delta t)_s$ is chosen as

$$\begin{gathered} \delta t = k(\delta t)_{\mathrm{ref}} + (\delta t)_{k+1} \qquad 0 < (\delta t)_{k+1} < (\delta t)_{\mathrm{ref}} \\ (\delta t)_s = \begin{cases} \delta t & \text{for } \delta t < (\delta t)_{\mathrm{ref}} \\ \frac{\delta t}{k+1} & \text{for } \delta t > (\delta t)_{\mathrm{ref}}, s = 1, 2, \ldots, k+1 \end{cases} \end{gathered} \tag{33}$$

For every single sub-time step $(\delta t)_s$:

(*a*) Use the updated pressure and temperature fields to solve the momentum equations.
(*b*) Substitute the new velocities into the pressure-correction equation and then solve the pressure-correction equation to update the velocity and pressure magnitudes, which satisfy the mass conservation law.
(*c*) Use the updated velocity vector to solve for the temperature.
(*d*) Go to step (a).

Repeat this procedure until the values of pressure, temperature, and velocity converge to the user specified tolerance.

3. Go to step 1 for the next time step. If the solid phase cannot move farther into a mushy cell, then stop the solidification process.

4. NUMERICAL EXAMPLES

Two model problems are used to validate the present method. They are known as the 1-D solidification without consideration of the convection effect, and tin melting in a rectangular cavity heated from the side wall with consideration of convection effect. The first problem is also known as the analytic Stefan problem [14] and will be chosen to access the present method. The second problem has been studied numerically [4]. After validating these two benchmark tests, the gallium melting studied experimentally [1] and numerically [2–4, 11, 13, 15, 16] is investigated. However, the numerical result was not consistent with the experimental results. The discrepancy is associated with the myth of grid-converged solution in the sense that the coarse-grid solution obtained from the lower-order scheme agrees better with the experimental results than with the predicted fine-grid and high-order solution. This problem will be studied systematically using the present mushy cell tracking method to clarify whether the solution is physically correct.

4.1. Solidification of One-Region Problem without Convection

An example taken from [14, 21] is investigated for evaluating the quality of the predicted solid–liquid interface. The domain and the specified boundary conditions

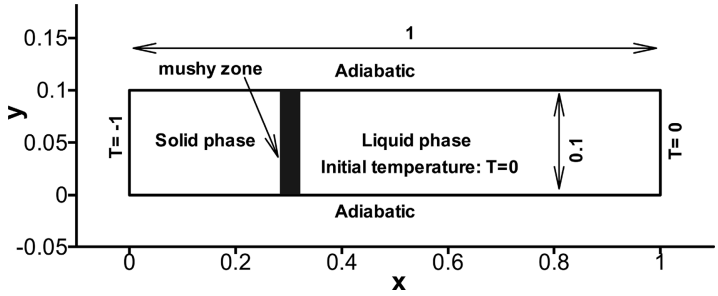

Figure 4. Schematic of the physical domain and the specified boundary conditions for the one-region problem.

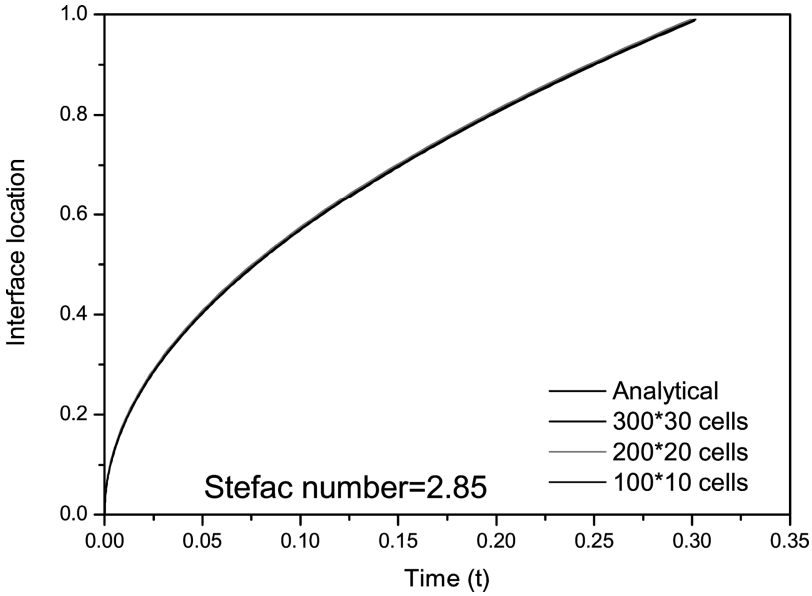

Figure 5. Comparison of the simulated and analytical interface locations for the investigated 1-D, one-region solidification problem (St = 2.85).

are shown in Figure 4. Three orthogonal and quadrilateral meshes with 100×10, 200×20, and 300×30 resolutions are selected for the current numerical simulation. Under $\rho_s = \rho_L = 1$, $k_s = k_L = 1$, and $C_s = C_L = 1$, the latent heat ΔH will be used

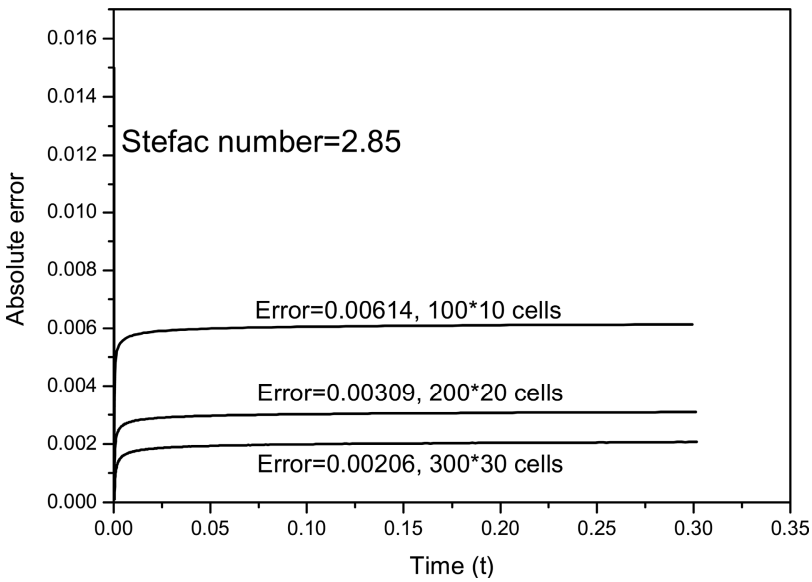

Figure 6. Simulated absolute errors for the numerical and analytical solid–liquid interface locations.

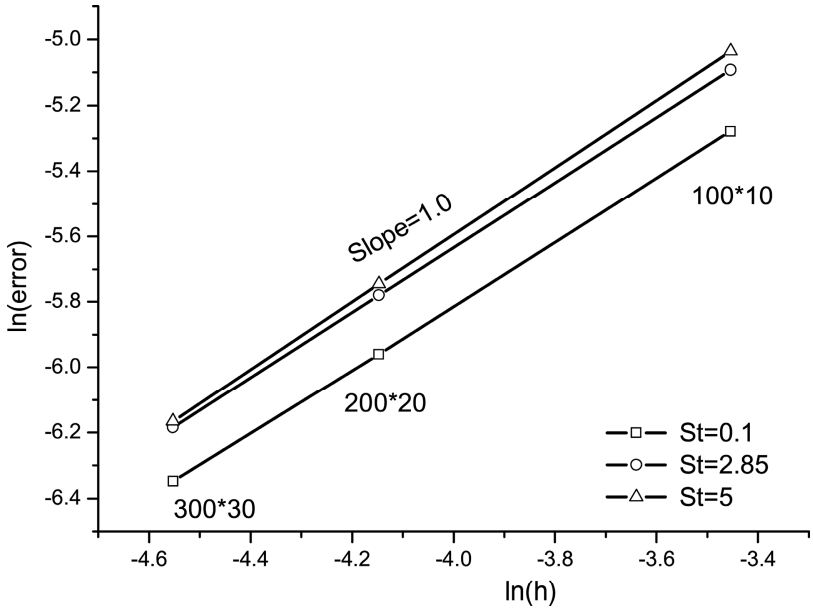

Figure 7. Simulated rates of convergence for the moving solid–liquid interface location.

to adjust the Stefan number St, which is defined as $\mathrm{St} = C_s(T_f - T_{\mathrm{surf}})/\Delta H$. Initially, the liquid in the domain under investigation is at rest and its temperature is kept at the freezing (or melting) temperature $T_f = 0$. The wall at $x = 0$ is maintained at the constant temperature $T_{\mathrm{surf}} = -1$. The resulting exact solution for the moving front is derived as $S(t) = \eta\sqrt{t}$ in the Appendix. The current simulations were performed at the Stefan numbers of 0.1, 2.85, and 5. The resulting values of η turn out to be 0.4400, 1.7985, and 2.1194, respectively. The simulated results for $S(t)$ at the Stefan number 2.85 are shown in Figure 5. Clearly, the simulated results and the analytical solutions are perfectly matched in the sense that the predicted discrepancy, defined as $\varepsilon \equiv \left|S(t)_{\mathrm{num}} - S(t)_{\mathrm{analytic}}\right|$, is negligibly small as shown in Figures 5 and 6. The accuracy order is determined according to the relation $\varepsilon \approx C(t)h^n$, where h is defined as the characteristic length of a cell. Figure 7 shows that the value of n is very close to 1, which can be also seen in Table 1. In other words, the error of the predicted interface location using the cell-by-cell thermally driven mushy cell tracking method is bounded by $\varepsilon \approx O(h)$. The results obtained at different Stefan numbers are summarized in Table 1.

Table 1. Absolute errors obtained at different Stefan numbers [14, 21]

Mesh	$\varepsilon(\mathrm{St} = 0.1)$	$\varepsilon(\mathrm{St} = 2.85)$	$\varepsilon(\mathrm{St} = 5)$
100×10	0.00510	0.00614	0.0065
200×20	0.00258	0.00309	0.0032
300×30	0.00175	0.00206	0.0021
	$S(t)_{\mathrm{analytic}} = 0.4400\sqrt{t}$	$S(t)_{\mathrm{analytic}} = 1.7985\sqrt{t}$	$S(t)_{\mathrm{analytic}} = 2.1194\sqrt{t}$

Table 2. Physical data for tin [4]

Symbol	ρ	k	C_p	μ	T_m	ρgβ	β	H
Units	kg/m^3	w/m K	J/kg K	NS/m	°C	kg/m^3 m/S^2 1/K	1/K	J/kg
Solid	7,500	60	200					
Liquid	7,500	60	200	6×10^{-3}	231.9	19.1	2.67×10^{-4}	6×10^4

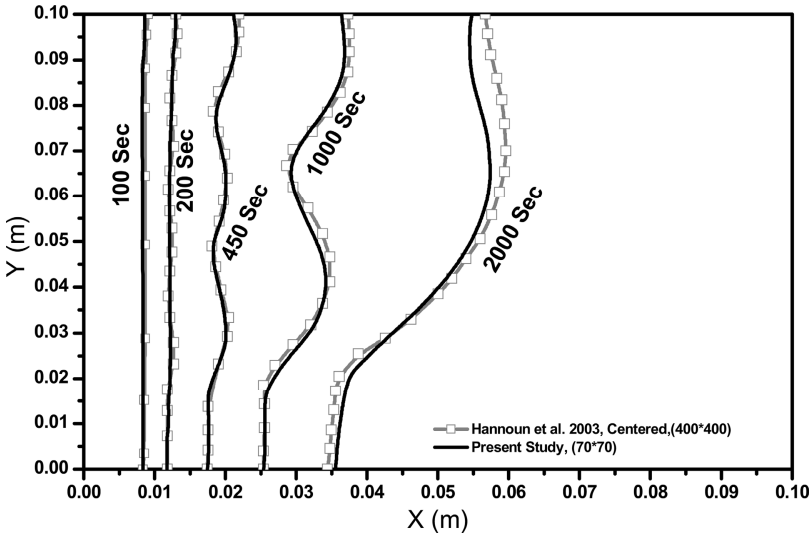

Figure 8. Comparison of the moving fronts during the melting of tin.

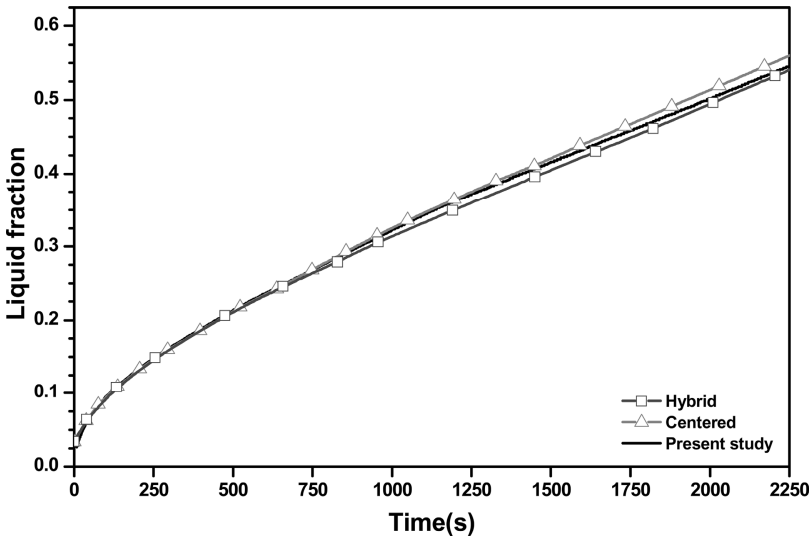

Figure 9. Simulated liquid fractions during the melting of tin (cells: 70 × 70).

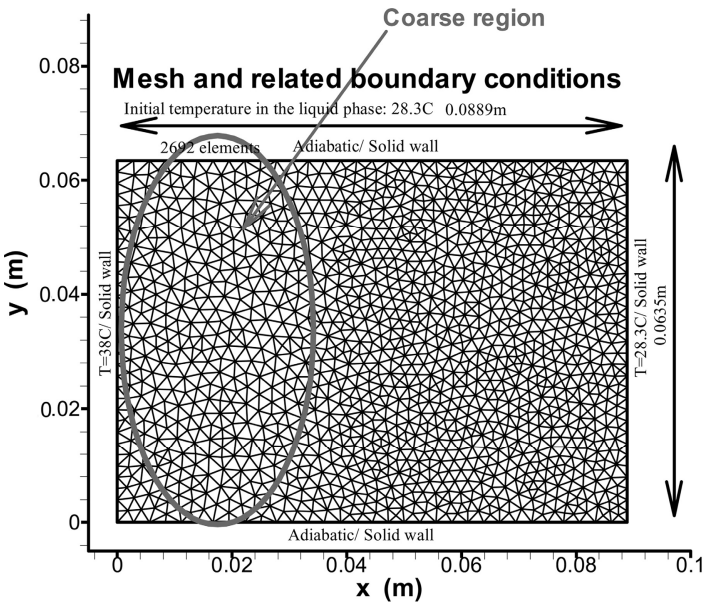

(a) Unstructured and coarse meshes

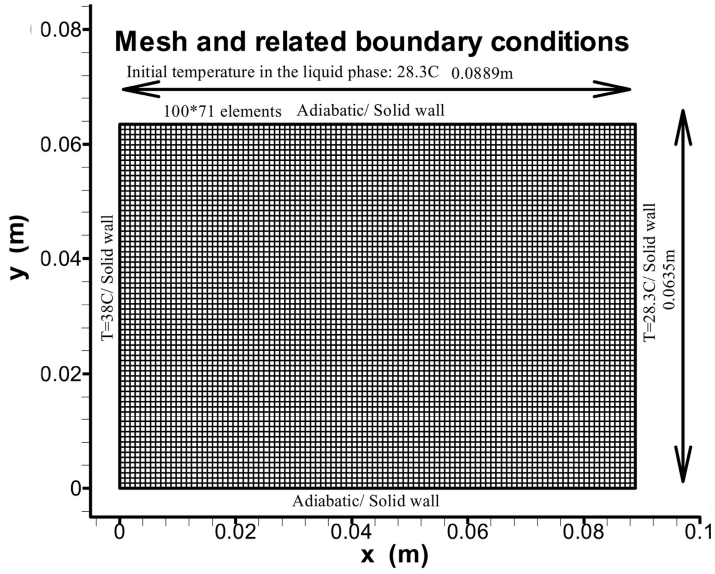

(b) Structured and fine meshes

Figure 10. Boundary conditions and computational meshes for simulating gallium melting: (*a*) unstructured/coarse meshes; (*b*) structured/fine meshes.

Table 3 Physical properties of gallium [4, 20]

Symbol	ρ	k	C_p	μ	T_m	ρgβ	β	H
Units	kg/m^3	w/m K	J/kg K	NS/m	°C	kg/m^3 m/S^2 1/K	1/K	J/kg
Solid	6,095	33.5	395.15	0				
Liquid	6,095	33.5	395.15	1.8×10^{-3}	29.78	7.0	1.173×10^{-4}	8×10^4

4.2. Melting of Tin

The melting of tin in a square cavity will be investigated at the published physical data [4] listed in Table 2. The left and right wall temperatures are 508 K and 505 K, respectively, and the bottom and top boundaries are assumed to be thermally adiabatic. The melting temperature of tin is assumed to be 505 K. The computed results regarding the moving front location and the liquid fraction compare all well with those given in [4], as shown in Figure 8 and Figure 9.

4.3. Melting of Gallium

Gallium melting in a rectangular cavity heated from the side wall has been studied experimentally [1] and numerically [2–4, 11, 13, 15, 16]. The widely cited experimental results of Gau and Viskanta [1] is chosen for the verification of the present numerical model. The geometric configuration and boundary conditions are sketched in Figure 10. Initially, the temperature in the solid gallium block is set at $T = 28.3$°C. The temperature at the left wall is increased instantly to $T = 38.0$°C, while the right wall temperature remains unchanged with the initial value of $T = 28.3$°C. The physical properties used in the current calculations are tabulated in Table 3 [4, 20].

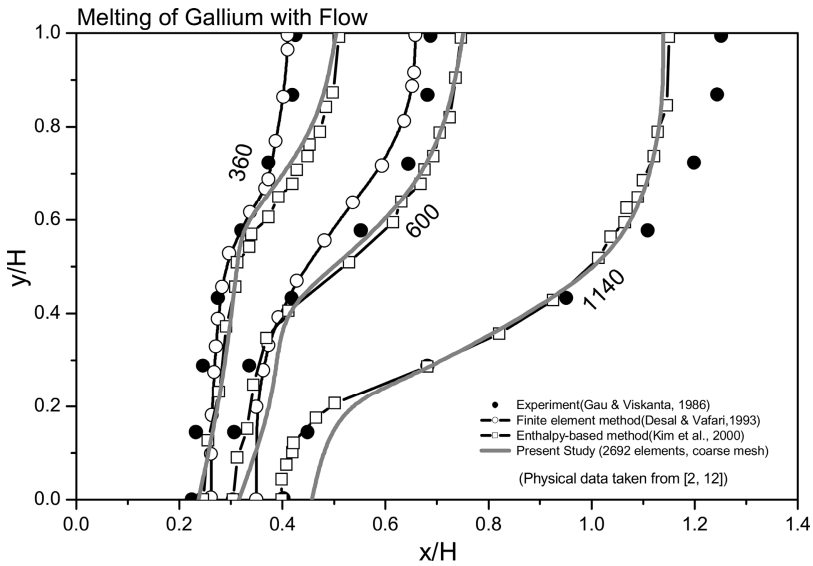

Figure 11. Comparison of the moving interfaces of gallium melting at various time instances.

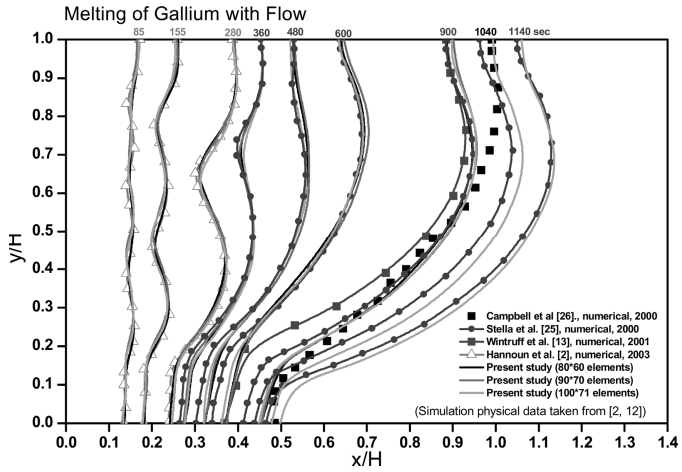

Figure 12. Comparison of the present result with other numerical results.

Hannoun et al. [4] employed the enthalpy method, together with various discretization schemes and grid resolutions, to study this problem. They found that the predicated dynamics of interface and thermofluid in the coarse meshes match better with the experimental data than those obtained from the fine meshes. In order to shed some light on this controversial prediction, several grid resolutions of unstructured and structured meshes as depicted in Figure 10 are employed. The coarse meshes generated around the interface region are very important, since they will

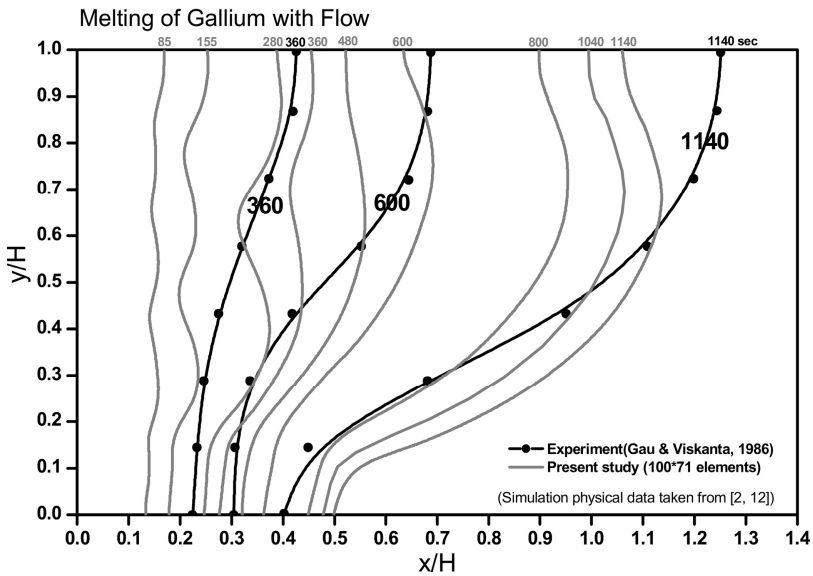

Figure 13. Comparison of the present result with the experimental data [1].

affect the simulated results, as noted by Hannoun et al. [4]. The resulting predicated solutions in the coarse meshes near the interface region can yield better prediction quality compared with the experimental data [1] and other numerical results [2, 3, 11] shown in Figure 11.

To further address the effect of mesh resolution on the predicted thermofluid flow field and interface dynamics, 80×60, 90×70, and 100×71 orthogonal, quadrilateral meshes are used. Comparison of the currently predicted interface with other numerical results is shown in Figure 12. The currently predicted interface matches well with the numerical results of Hannoun et al. [4] in the early period of simulation ($t < 280$ s) and agrees well with the other numerical results for $t > 360$ s, as shown in

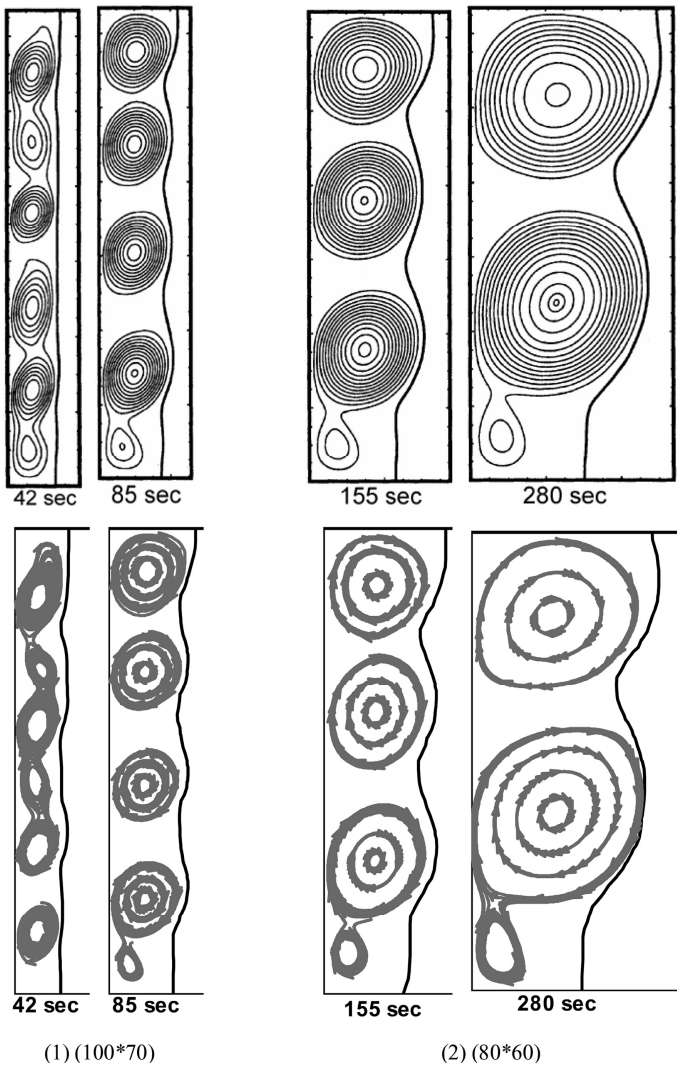

Figure 14. Simulated streamlines: upper row from [4] and lower row from the present study.

Figure 12. Comparison of the numerical results with the experimental data [1] is depicted in Figure 13. The discrepancy between the numerical result and those obtained from the fine meshes and the experimental data is significant and has been discussed by Hannoun et al. [4]. This predicted difference might be attributed to the discrepancy between the experimental setup and the assumptions made in the numerical simulation. The corresponding streamline patterns obtained at various time instants are shown in Figure 14.

5. CONCLUSIONS

A thermally driven mushy cell tracking solution algorithm has been developed within the finite-volume context. The physical domain is separated into solid-phase and liquid-phase regions, with the mushy cells being placed in between. The mushy cell tracking equation has been derived to satisfy the mass and energy conservations so as to be able to accurately predict the movement of the mushy cells. Both 1-D solidification without convection transport, and tin and gallium 2-D melting with convection have been studied to validate the method. Based on the computed results, the following conclusions can be drawn.

1. Simulation of the solidification shows that the predicted moving interface $S(t)$ agrees well with the analytic solution. The predication accuracy order for the moving interface is linear in the sense that $\varepsilon(t) \approx C(t)h$. This finding is close to the order of accuracy predicted by the moving-particle method [12].
2. As Hannoun et al. [4] demonstrated, our gallium melting interface, predicted in the coarse meshes, near the interface region matches better with the experimental data [1] and other numerical results [2, 3, 11]. We believe these predictions are mesh-dependent, but the mesh resolution is not fine enough to resolve the small and complex thermofluid flow field structure near the top wall close to the interface area. Simulation of gallium melting in fine meshes shows that the predicted thermofluid flow field and dynamics of mushy cells agree well with the experimental data [1] and other numerical results [4, 11, 15, 16] in the early simulation period ($t = 0$–280 s). The simulated results are different from the experimental data but are consistent with other numerical results in the later period of simulation ($t > 360$ s). The discrepancy between the experimental and numerical results might be attributed to the experimental setup, which is not consistent with the assumptions made in the numerical simulation, as elaborated in [4].

REFERENCES

1. C. Gau and R. Viskanta, Melting and Solidification of a Pure Metal on a Vertical Wall, *Trans. ASME, J. Heat Transfer*, vol. 108, pp. 174–181, 1986.
2. C. P. Desai and K. Vafai, A Unified Examination of the Melting Process within a Two-Dimensional Rectangular Cavity, *Trans. ASME, J. Heat Transfer*, vol. 115, pp. 1072–1075, 1993.
3. R. Viswanath and Y. Jaluria, A Comparison of Different Solution Methodologies for Melting and Solidification Problems, *Numer. Heat Transfer B*, vol. 24, pp. 77–105, 1993.

4. N. Hannoun, V. Alexiades, and T. Z. Mai, Resolving the Controversy over Tin and Gallium Melting in a Rectangular Cavity Heated from the Side, *Numer. Heat Transfer B*, vol. 44, pp. 253–276, 2003.
5. Y. J. Jan, A Cell-by-Cell Thermally Driven Mushy Cell Tracking Algorithm for Phase-Change Problems—Part I: Concept for Tracking the Moving Front, *J. Comput. Mech.*, in press, 2006.
6. Y. J. Jan, A Cell-by-Cell Thermally Driven Mushy Cell Tracking Algorithm for Phase-Change Problems—Part II: Phase-Change with Natural Convection, *J. Comput. Mech.*, in press, 2006.
7. W. Shyy, H. S. Udaykumar, M. M. Rao, and R. W. Smith, *Computational Fluid Dynamics with Moving Boundaries*, Taylor & Francis, Washington, DC, 1996.
8. W. Shyy, S. S. Thakur, H. Ouyang, J. Liu, and E. Blosch, *Computational Techniques for Complex Transport Phenomena*, Cambridge University Press, Cambridge, UK, 1997.
9. J. Crank, *Free and Moving Boundary Problems*, Oxford University Press, Oxford, UK, 1984.
10. A. D. Brent, V. R. Voller, and K. J. Reid, Enthalpy-Porosity Technique for Modeling Convection-Diffusion Phase-Change: Application to the Melting of a Pure Metal, *Numer. Heat Transfer*, vol. 13, pp. 297–318, 1988.
11. S. Kim, S. Anghaie, and G. Chen, A Fixed-Grid Two-Phase Numerical Model for Convection-Dominated Melting and Solidification, *Trends in Numerical and Physical Modeling for Industrial Multiphase Flows*, pp. 27–29, Institut d'Etudes Scientifiques de Cargèse, France, 2000.
12. H. S. Udaykumar, R. Mittal, and W. Shyy, Computation of Solid-Liquid Phase Fronts in the Sharp Interface Limit on the Fixed Grids, *J. Comput. Phys.*, vol. 153, pp. 535–574, 1999.
13. I. Wintruff, C. Giinther, and A. G. Class, An Interface-Tracking Control-Volume Finite-Element Method for Melting and Solidification Problems—Part II: Verification and Application, *Numer. Heat Transfer B*, vol. 39, pp. 127–149, 2001.
14. M. N. Ozisik, *Heat Conduction*, Wiley, New York, 1980.
15. F. Stella and M. Giangi, Melting of a Pure Metal on a Vertical Wall: Numerical Simulation, *Numer. Heat Transfer A*, vol. 38, pp. 193–208, 2000.
16. T. A. Campbell and J. N. Koster, Visualization of Liquid/Solid Interface Morphology in Gallium Subject to Natural Convection, *J. Crystal Growth*, vol. 140, pp. 414–425, 1994.
17. J. H. Ferziger and M. Peric, *Computational Methods for Fluid Dynamics*, Springer-Verlag, Berlin, 1999.
18. B. R. Baliga and S. V. Patankar, A Control-Volume Finite Element Method for Two-Dimensional Fluid Flow and Heat Transfer, *Numer. Heat Transfer*, vol. 6, pp. 245–261, 1983.
19. Y. Saad, *Iterative Methods for Sparse Linear Systems*, PWS Publishing, Boston, 1996.
20. R. Sampath and N. Zabaras, An Object-Oriented Implementation of a Front Tracking Finite Element Method for Directional Solidification Processes, *Int. J. Numer. Meth. Eng.*, vol. 44, pp. 1227–1265, 1999.
21. C. Y. Li, S. V. Garimella, and J. F. Simpson, Fixed-Grid Front-Tracking Algorithm for Solidification Problems—Part I: Method and Validation, *Numer. Heat Transfer B*, vol. 43, pp. 117–141, 2003.
22. Y. J. Jan, Thermally Driven Mushy Cell Tracking Algorithm for Dendritic Solidification, Numer. Heat Transfer, B, accepted, 2007.
23. S. R. Mathur and J. Y. Murthy, A Pressure-Based Method for Unstructured Meshes, *Numer. Heat Transfer B*, vol. 31, pp. 195–215, 1997.
24. P. A. Jayantha and I. W. Turner, A Comparison of Gradient Approximations for Use in Finite-Volume Computational Models for Two-Dimensional Diffusion Equations, *Numer. Heat Transfer B*, vol. 40, pp. 367–390, 2001.

25. G. Labonia, V. Timchenko, J. E. Simpson, S. V. Garimella, E. Leonardi, and G. De Vahl Davis, Reconstruction and advection of a moving interface in three dimensions on a fixed grid, *Numer. Heat Transfer B*, vol. 34, pp. 121–138, 1998.
26. P. Jawahar and H. Kamath, A High-Resolution Procedure for Euler and Navier-Stokes Computations on Unstructured Grids, *J. Comput. Phys.*, vol. 164, pp. 165–203, 2000.
27. S. Kang and Y. Kim, Pressure Based Unstructured Grid Finite Volume Method for Simulating Laminar Reacting Flows, *Numer. Heat Transfer B*, vol. 41, pp. 53–72, 2002.
28. C. M. Rhie and W. L. Chow, Numerical Study of the Turbulent Flow Past an Airfoil with Training Edge Separation, *AIAA J.*, vol. 21, pp. 1525–1532, 1983.

APPENDIX: EVALUATION OF THE MOVING-FRONT LOCATION

Consider the following one-dimensional equation:

$$\frac{\partial T}{\partial t} = \frac{k_s}{\rho_s C_s}\frac{\partial^2 T}{\partial x^2} \qquad 0 < x < H$$
$$\begin{cases} t = 0, & T = T_m \\ x = 0, & T = T_{\text{surf}} \\ x = S(t), & T = T_m \end{cases} \tag{A1}$$

where $S(t)$ is the interface between the liquid and solid phase. In Eq. (A1), the particular solution is given as

$$T - T_m = C_1\left[\operatorname{erf}(a) - \operatorname{erf}\left(\frac{x}{\sqrt{4\alpha_s t}}\right)\right] \tag{A2}$$

Note that erf(a) is defined as $\operatorname{erf}(a) = 2\int_0^a (e^{-\eta^2})\,d\eta/\sqrt{\pi}$ and the thermal diffusivity is defined as $\alpha_s \equiv k_s/\rho_s C_s$. The subscript s represents the solid phase. Two constants, C_1 and a, could be specified by substituting the boundary conditions into Eq. (A2) to render $T_{\text{surf}} - T_m = C_1 \operatorname{erf}(a)$ and $a = S(t)/\sqrt{4\alpha_s t}$. It should be noted that $dT\,[\equiv (\partial T/\partial t)\,dt + (\partial T/\partial x)\,dx]$ at the moving front is zero for the constant-melting or frozen-temperature case. Thus,

$$\left(\frac{\partial T}{\partial t}\right)_{x=S(t)} = -\frac{dx}{dt}\left[\left(\frac{\partial T}{\partial x}\right)\right]_{x=S(t)}$$

results. Thanks to the energy conservation principle, we can get

$$\left(\frac{dx}{dt}\right)_{x=S(t)} = \frac{\alpha_s C_s}{(\Delta H)}\left(\frac{\partial T}{\partial x}\right)_{x=S(t)}$$

in the one-dimensional domain. Note that ΔH is the latent heat of the phase change and C_s is the heat capacity for the solid. Consequently, the equation for the moving interface can be described as

$$\left(\frac{\partial T}{\partial t}\right)_{x=S(t)} = -\frac{\alpha_s C_s}{(\Delta H)}\left[\left(\frac{\partial T}{\partial x}\right)^2\right]_{x=S(t)} \tag{A3}$$

Since $(\partial T/\partial t)_{x=S(t)}$ and $(\partial T/\partial x)_{x=S(t)}$ can be respectively expressed as

$$\left(\frac{\partial T}{\partial t}\right)_{x=S(t)} = \frac{C_1 S(t)}{\sqrt{4\alpha_s \pi t^3}} e^{-S(t)^2/4\alpha_s t} \tag{A4}$$

$$\left(\frac{\partial T}{\partial x}\right)_{x=S(t)} = \frac{C_1}{\sqrt{\alpha_s \pi t}} e^{-S(t)^2/4\alpha_s t} \tag{A5}$$

we can have

$$C_1 = -\frac{(\Delta H) a\sqrt{\pi}}{C_s}\left(e^{a^2}\right) \tag{A6}$$

By substituting Eq. (A6) into the equation given by $T_{\text{surf}} - T_m = C_1 \operatorname{erf}(a)$, we are led to derive $T_{\text{surf}} - T_m = -(\Delta H) a\sqrt{\pi}\left(e^{a^2}\right) \operatorname{erf}(a)/C_s$.

To further illustrate the time-varying front feature, the Taylor series approximation is applied to $ae^{a^2} \operatorname{erf}(a)$, thus resulting in

$$\begin{aligned} ae^{a^2} \operatorname{erf}(a) &= \frac{2a^2}{\sqrt{\pi}}\left(1 + a^2 + \frac{a^4}{2} + \cdots\right)\left(1 - \frac{a^2}{3 \times 1!} + \frac{a^4}{5 \times 2!} - \cdots\right) \\ &= \frac{2a^2}{\sqrt{\pi}}\left(1 + \frac{2}{3}a^2 + \frac{4}{15}a^4 + \cdots\right) \end{aligned} \tag{A7}$$

A further simplification of $T_{\text{surf}} - T_m$ can render

$$T_{\text{surf}} - T_m = -\frac{2(\Delta H)a^2}{C_s}\left(1 + \frac{2}{3}a^2 + \frac{4}{15}a^4 + \cdots\right) \tag{A8}$$

The Stefan number is defined as $\text{St} \equiv -(T_{\text{surf}} - T_m)C_s/\Delta H$ and its value is obtained from $\text{St} = 2a^2\left(1 + 2a^2/3 + \cdots\right)$ for solidification. The Stefan number is defined to signify the importance of the sensible heat relative to the latent heat. If we keep the term $(a)^2 2/3$, the accurate front profile $S(t)$ can be approximated as below after some simple calculations.

$$\begin{aligned} S &= \left[\sqrt{-3 + \sqrt{9 + 12\left(\frac{(T_m - T_{\text{surf}})C_s}{\Delta H}\right)}}\right]\sqrt{\alpha_s t} \\ &= \left[\sqrt{-3 + \sqrt{9 + 12(\text{St})}}\right]\sqrt{\alpha_s t} \\ &= \eta\sqrt{t} \end{aligned} \tag{A9}$$

If the simulation is performed at $\text{St} = 0.1$, the values of η becomes 0.4400.